Supplement of Atmos. Chem. Phys., 26, 5477–5496, 2026
https://doi.org/10.5194/acp-26-5477-2026-supplement

Atmospheric Chemistry and Physics
Open Access
EGU

Supplement of

Observational insights into atmospheric CO_2 and CO at the urban canopy layer top in Metropolitan Shanghai, China

Shuang Fu et al.

Correspondence to: Shuangxi Fang (fangsx@zjut.edu.cn)

Table S1: Measured CO_2 mixing ratio (ppm) at different sites during nearly concurrent periods.

Observation Site	Category	Geography	Period	CO_2	Reference
Sutro Tower (STR), California, USA	Urban	122.45°W, 37.76°N; 254 m a.s.l	2021	420.47 ± 11.23	NOAA [a]
Yongsan Building (YSB), Seoul, South Korea	Urban	126.96°E, 37.52°N; 113 m a.s.l	2019/7–2020/9	442.99 ± 18.67	Park et al. (2021)
Lulin (LLN), Taibei, China	Regional background	120.87°E, 23.47°N; 2862 m a.s.l	2021	417.21 ± 3.43	NOAA [a]
King's Park (HKO), Hong Kong, China	Regional background	114.17°E, 22.31°N; 65 m a.s.l	2021	439.11 ± 6.87	NOAA [a]
Waliguan (WLG), China	Global background	100.54°E, 36.17°N; 3810 m a.s.l	2021/4–2023/3	418.95 ± 3.65	NOAA [a]
Mauna Loa (MLO), Hawaii, USA	Global background	155.58°W, 19.54°N; 3397 m a.s.l	2021/4–2023/3	418.12 ± 2.54; 417.80 ± 2.48	NOAA [a]
Cape Grim, Tasmania, Australia	Global background	144.70°E, 40.68°S; 94 m a.s.l	2021/4–2023/3	413.66 ± 1.34	NOAA [a]
Longfengshan (LFS), Harbin, Heilongjiang, China	Regional background	127.60°E, 44.73°N; 331 m a.s.l.	2021–2022	422.8 ± 0.5–424.9 ± 0.6	China GHG Bulletin[c]
Shangdianzi (SDZ), Beijing, China	Regional background	117.12°E, 40.65°N; 293.3 m a.s.l.	2021–2022	427.7 ± 0.4–428.7 ± 0.4	China GHG Bulletin [c]
Akedala station, Altay region, Xinjiang, China	Regional background	87.93°E, 47.10°N; 563.3 m a.s.l.	2019/11; 2021–2022	~ 410.43; 419.1 ± 0.6–421.4 ± 1.3	Zhao et al. (2022); China GHG Bulletin [c]
Lin'an (LAN), Zhejiang, China	Regional background	119.44°E, 30.18°N; 138.6 m a.s.l	2020/11–2021/10	441.56 ± 15.42	Chen et al. (2024)
Hangzhou (HZ), Zhejiang, China	Urban	120.17°E, 30.22°N; 41.7 m a.s.l	2020/11–2021/10	446.52 ± 17.01	Chen et al. (2024)
Jungfraujoch (JFJ), Switzerland	High-altitude mountain	7.99°E, 46.55°N; 3580 m a.s.l	2021/4–2023/3	418.30 ± 5.39	WDCGG [d]
Heathfield (HFD), United Kingdom	Regional background[#]	0.23°E, 50.98°N; 210 m a.s.l	2021–2023	424.84 ± 0.67	WDCGG [d]
Hohenpeissenberg (HPB), Germany	Global background[#]	11.01°E, 47.80°N; 1065 m a.s.l	2021–2023	421.01 ± 0.73	WDCGG [d]
Ispra (IPR), Italy	Regional background[#]	8.63°E, 45.80°N; 250 m a.s.l	2021–2023	438.67 ± 1.42	WDCGG [d]
Kresin u Pacova (KRE), Czech Republic	Regional background[#]	15.08°E, 49.58°N; 544 m a.s.l	2021–2023	427.05 ± 0.64	WDCGG [d]
Observatoire Pérenne de l'Environnement (OPE), France	Regional background[#]	5.50°E, 48.56°N; 400 m a.s.l	2021–2023	427.00 ± 0.75	WDCGG [d]
Saclay (SAC), France	Regional background[#]	2.14°E, 48.72°N; 175 m a.s.l	2021–2023	430.76 ± 1.31	WDCGG [d]
Torfhaus (TOH), Germany	Regional background[#]	10.53°E, 51.81°N; 948 m a.s.l	2021–2023	421.08 ± 0.57	WDCGG [d]
ABLECAS site, Zhejiang, China	High-altitude mountain	119.51°E, 28.58°N; 1128 m a.s.l	2022/7/10–2021/6/20	426.3 ± 10.0	Ye et al. (2024)
Damingshan (DMS), Zhejiang, China	High-altitude mountain	119.00°E, 30.01°N; 1489.9 m a.s.l	2020/11–2021/10; 2021/4–2022/12	422.02 ± 10.67; 419.38 ± 2.30[*]	Chen et al. (2024); This study
Shanghai Tower (SHT), Shanghai, China	Urban[#]	121.51°E, 31.23°N; 637.0 m a.s.l.	2021/4/17–2023/3/6	433.50 ± 0.33[*]	This study
			Spring	428.16 ± 0.45[*]	
			Summer	426.98 ± 0.49[*]	
			Autumn	437.55 ± 0.65[*]	
			Winter	440.73 ± 0.86[*]	
Global Annual Mean			2021–2022	415.7 ± 0.20–417.9 ± 0.20	WMO (2022, 2023) [b]

[a] Derived from NOAA (available at: https://gml. noaa.gov/dv/iadv/, last access: August 2025); [b] Retrieved from WMO Greenhouse Gas Bulletin, No. 18–26 &19–15 (available at: https://library.wmo.int/records/, last access: 9 September 2025); [c] Retrieved from China Greenhouse Gas Bulletin (available at: https://www.cma.gov.cn/zfxxgk/gknr/qxbg/, last access: 10 September 2025); [d] Derived from WDCGG (available at: https://gaw.kishou.go.jp/, last access: November 2025); [#] Based on the tower platform; [*]Values are presented as mean ± 95% CI for SHT and DMS, and as mean ± SD for other sites.

Table S2: Observed CO_2 (ppm) and CO (ppb) mole fractions at the SHT site and their relative excesses above background levels.

Periods	**CO_2**	**$CO_{2,\,bk}$**	**$CO_{2,\,ex}$** (ff; bio-dominated)	**CO**	**CO_{bk}**	**CO_{ex}**
Spring	427.7 ± 12.7	423.2 ± 7.9	4.4 (3.7; 0.7)	199.7 ± 138.0	162.5 ± 92.1	37.2
Summer	424.9 ± 12.0	420.5 ± 5.8	4.4 (6.4; –2.0)	252.3 ± 187.3	152.3 ± 65.6	100.0
Autumn	437.2 ± 19.4	428.9 ± 10.0	8.3 (7.1; 1.2)	428.5 ± 346.3	281.1 ± 162.9	147.4
Winter	443.8 ± 24.5	432.4 ± 15.5	11.4 (8.3; 3.1)	387.1 ± 304.5	278.3 ± 170.9	108.7
No-rain periods	434.4 ± 19.9	426.9 ± 11.7	7.5 (6.4; 1.1)	325.7 ± 283.4	226.8 ± 149.3	98.9

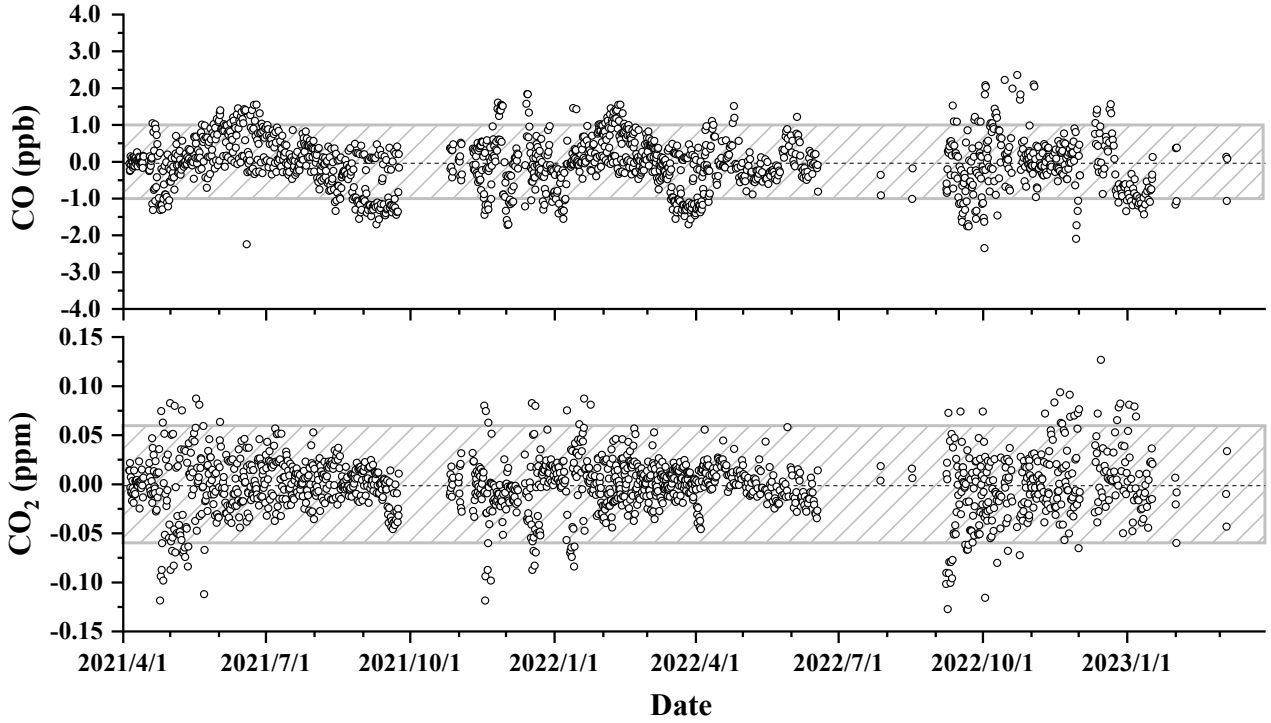

Figure S1: Differences of the measured and assigned CO and CO_2 mole fractions for the target gas (T) during the observation period. The gray shaded area represents the ±1σ range.

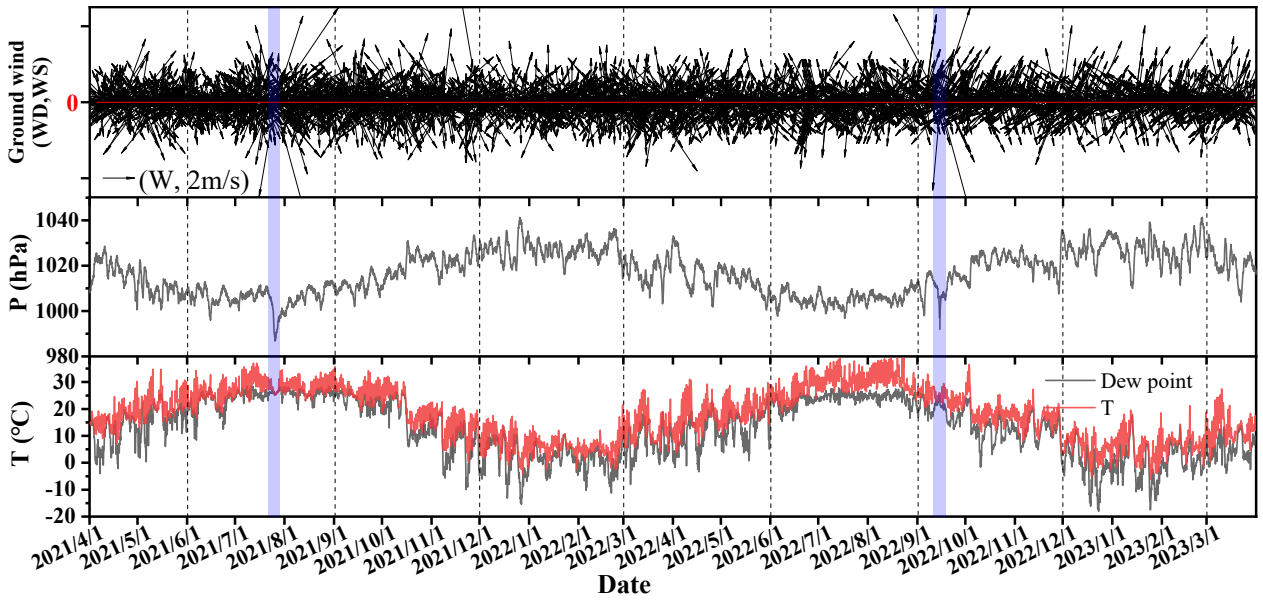

Figure S2: The time series of the ground wind, air pressure and temperature during this campaign with a 3-h time resolution from Baoshan Meteorological Station (BS; 31.23°N, 121.29°E; 20.9 km from SHT). Blue shaded areas mark typhoon events (July 25–26, 2021, and September 14–15, 2022).

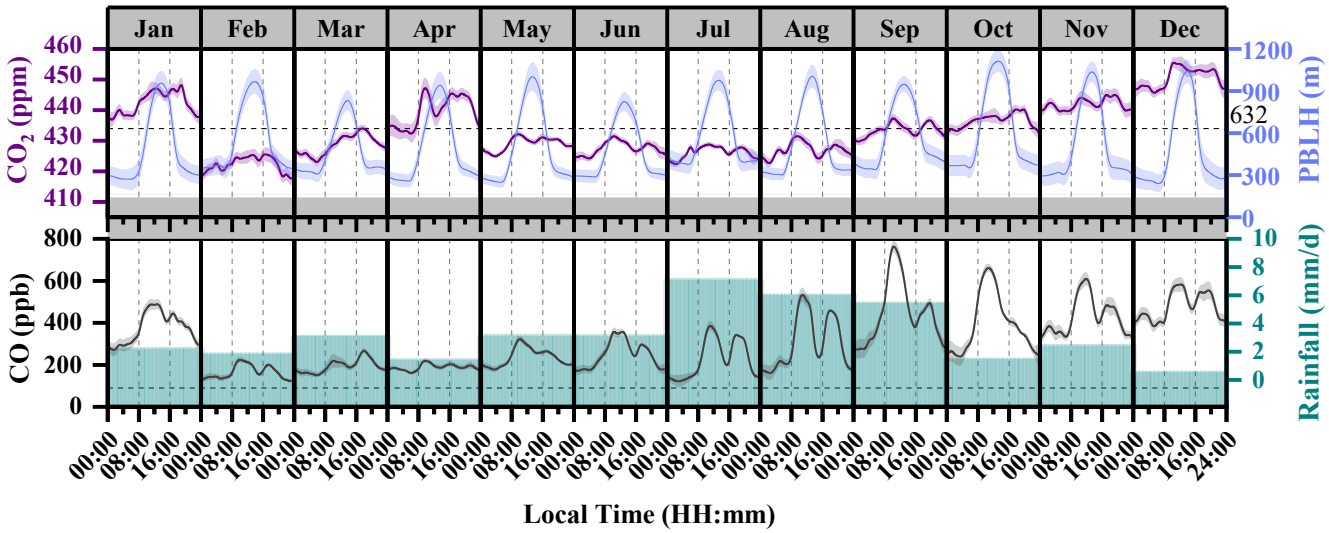

Figure S3: Diurnal cycles for various species and parameters for different months during the campaign at SHT site. Rainfall data were processed from the BS station at 6-h intervals.

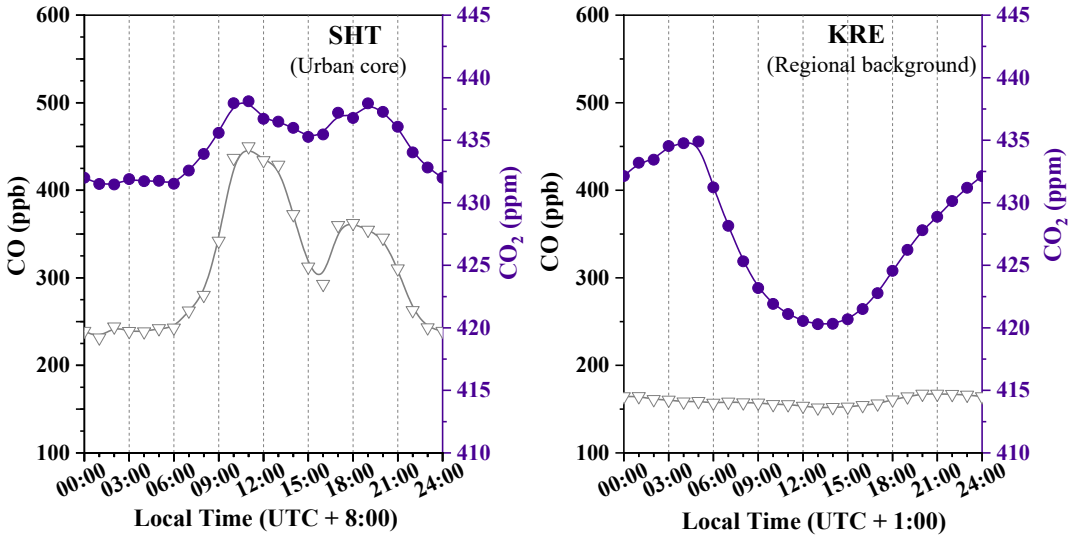

Figure S4: Diurnal cycles of CO and CO_2 observed at the SHT (urban core elevated site) and the KRE (background tall tower). See Table S1 for the site details.

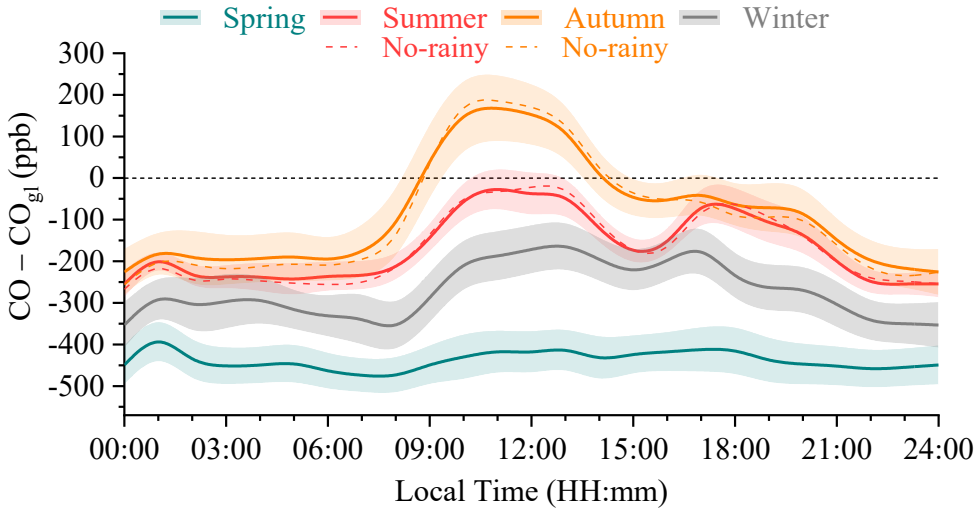

Figure S5: The variations on concentration differences of CO between the tower top (expressed as CO_{st} here) and the ground (CO_{gl}).

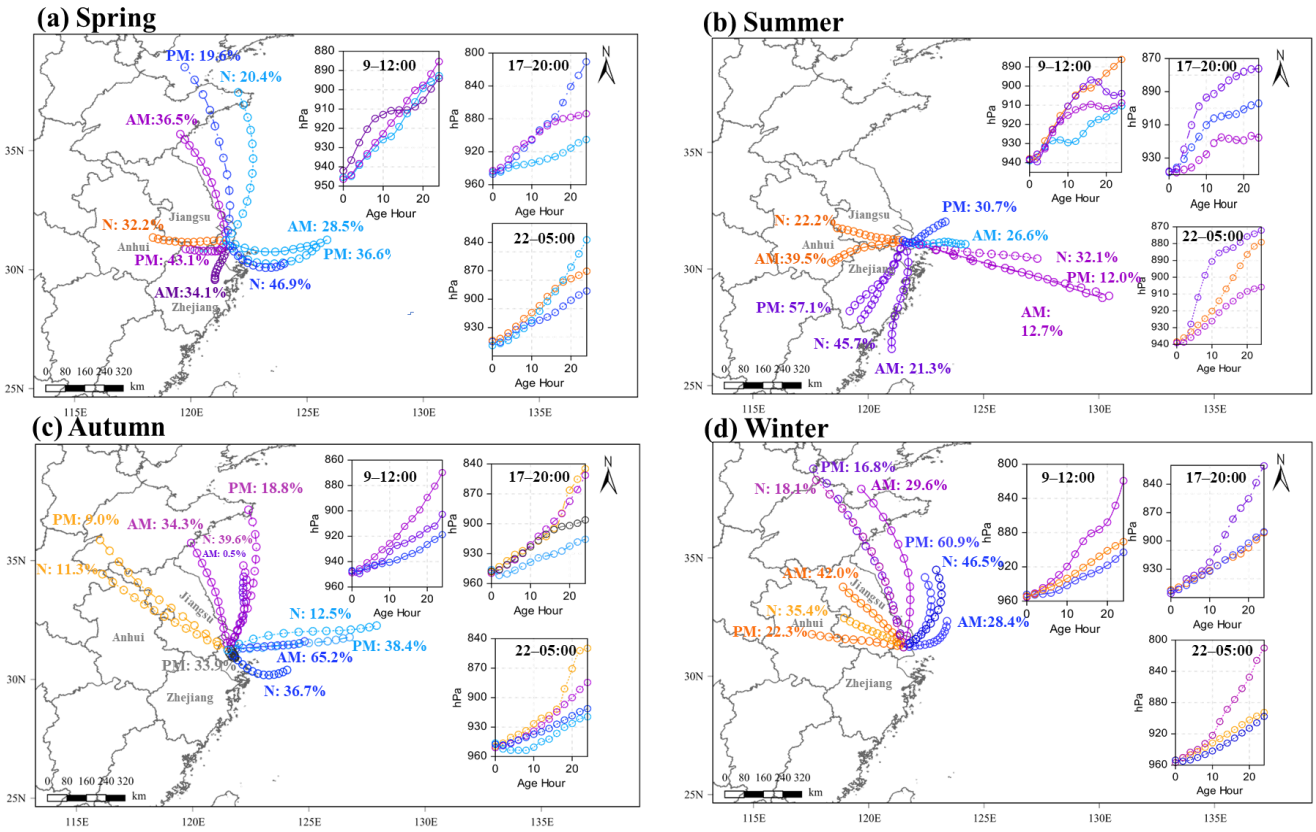

Figure S6: Cluster analysis of the 24-h back trajectories at SHT site for the AM (9:00–12:00), PM (17:00–20:00), and N (22:00–05:00) periods.

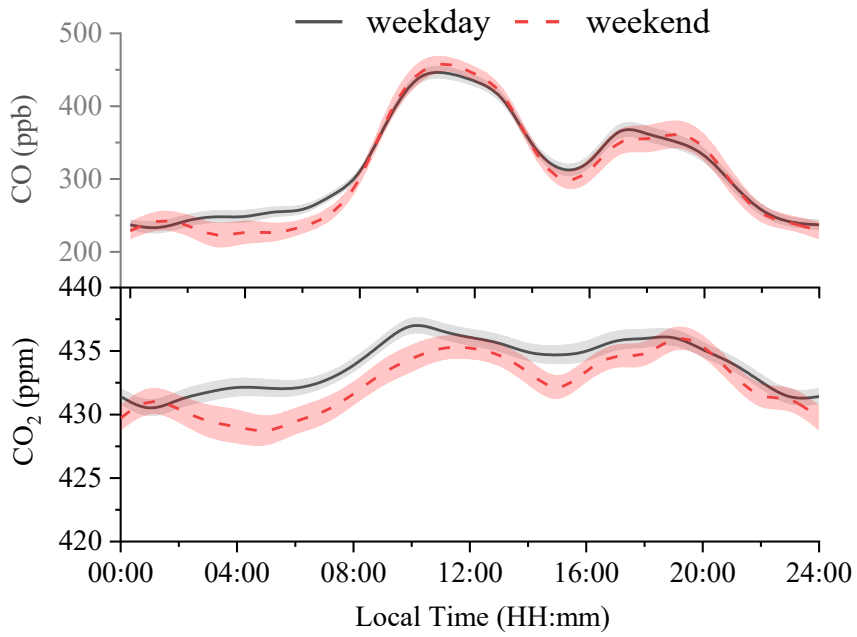

Figure S7: The diurnal variations of atmospheric CO_2 and CO between weekdays and weekends at the SHT site.

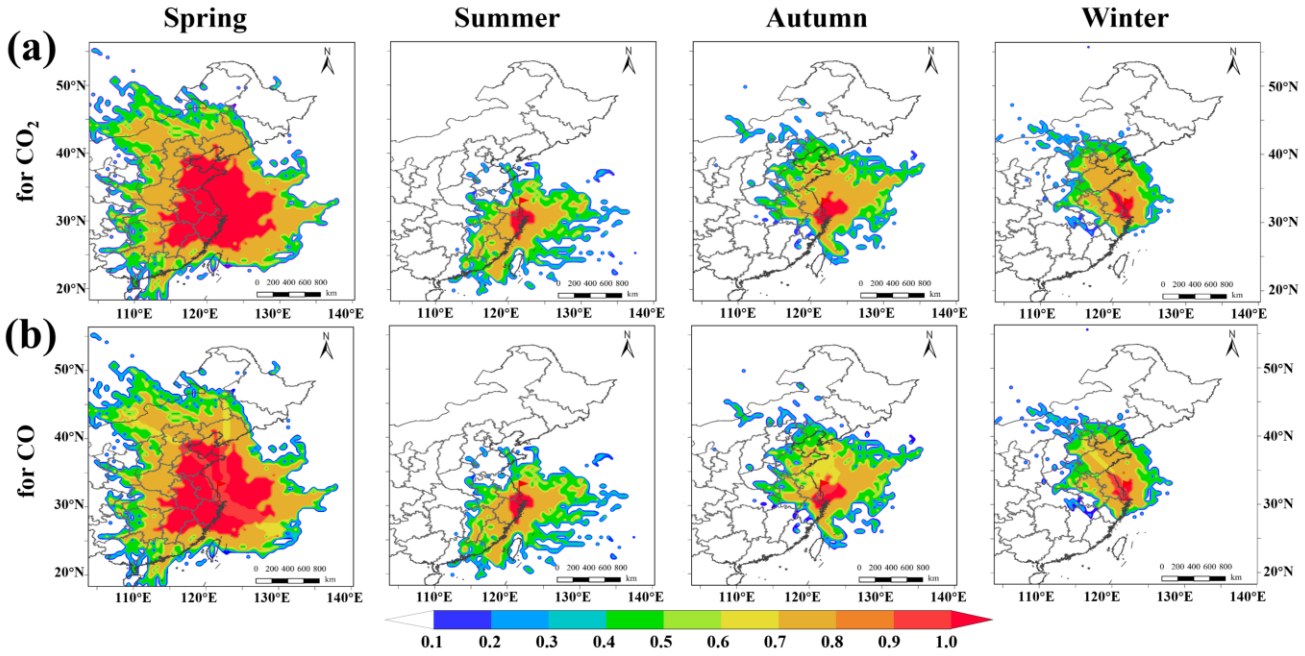

Figure S8: The spatial contribution of potential sources using the Weighted Potential Source Contribution Function (WPSCF; see main text Section 2.2) based on 3-day back trajectories.

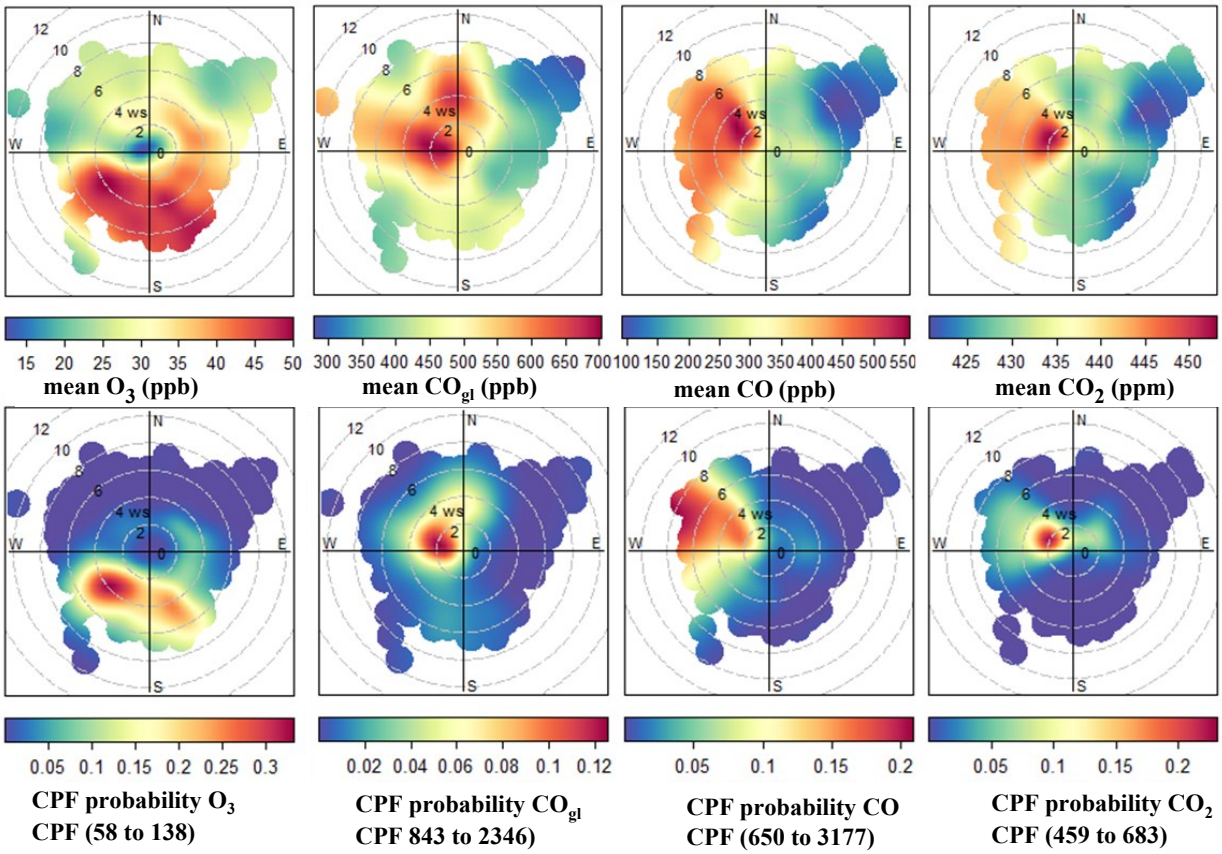

Figure S9: The wind rose plots of ground-level O_3 and CO, and tower-top CO and CO_2 measurements and the corresponding Conditional Probability Function (CPF) statistics for their upper 10% values.

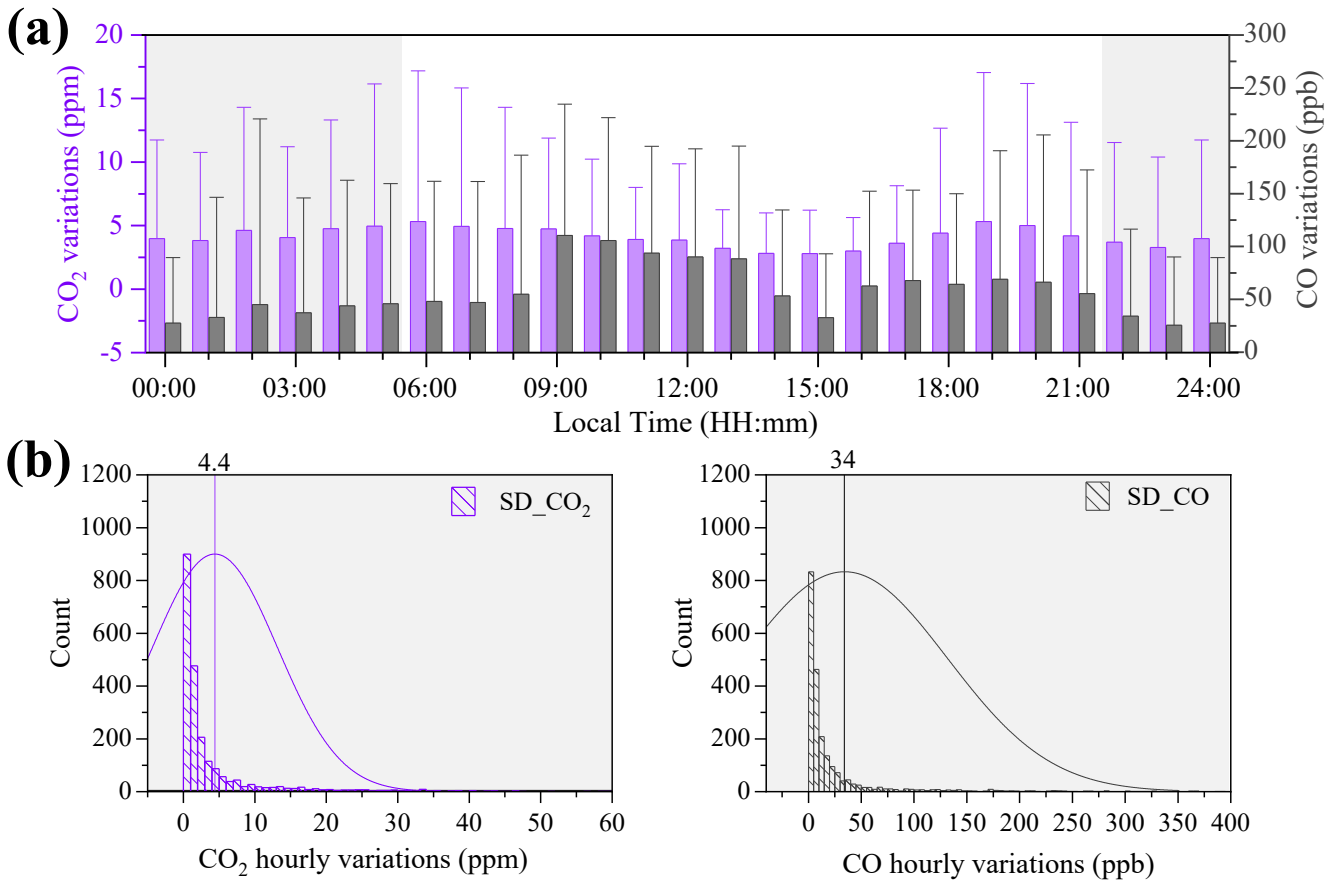

Figure S10: Mean diurnal cycles of CO_2 and CO variations (hourly standard deviation, SD, at SHT) and their distributions based on 1-h resolution data.

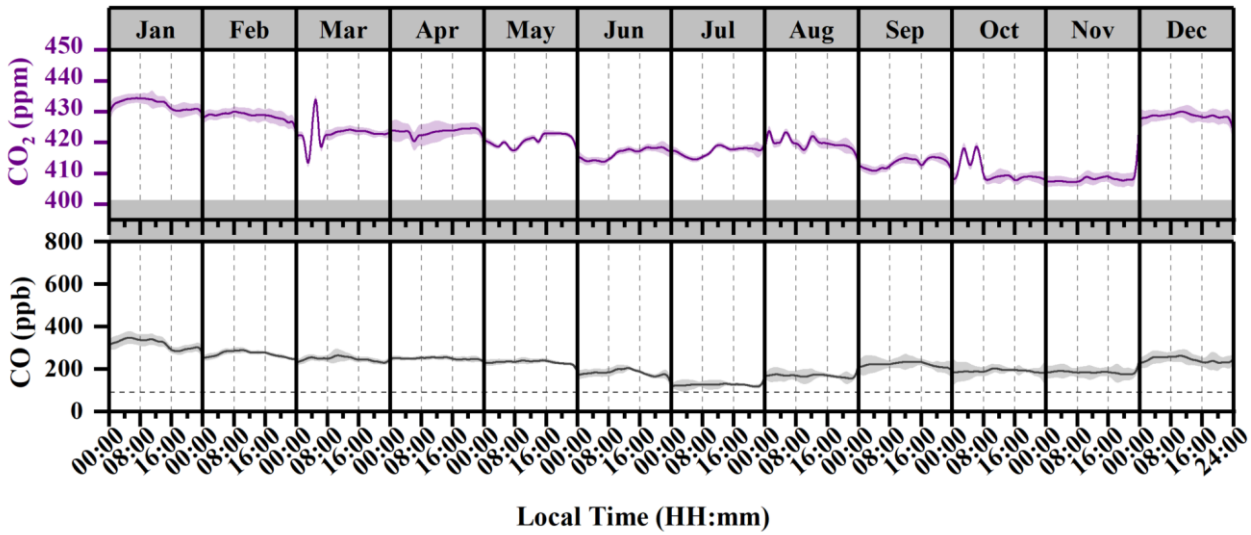

Figure S11: The averaged diurnal cycles of atmospheric CO_2 and CO concentrations over different months measured at the DMS site during April 2021–December 2022.

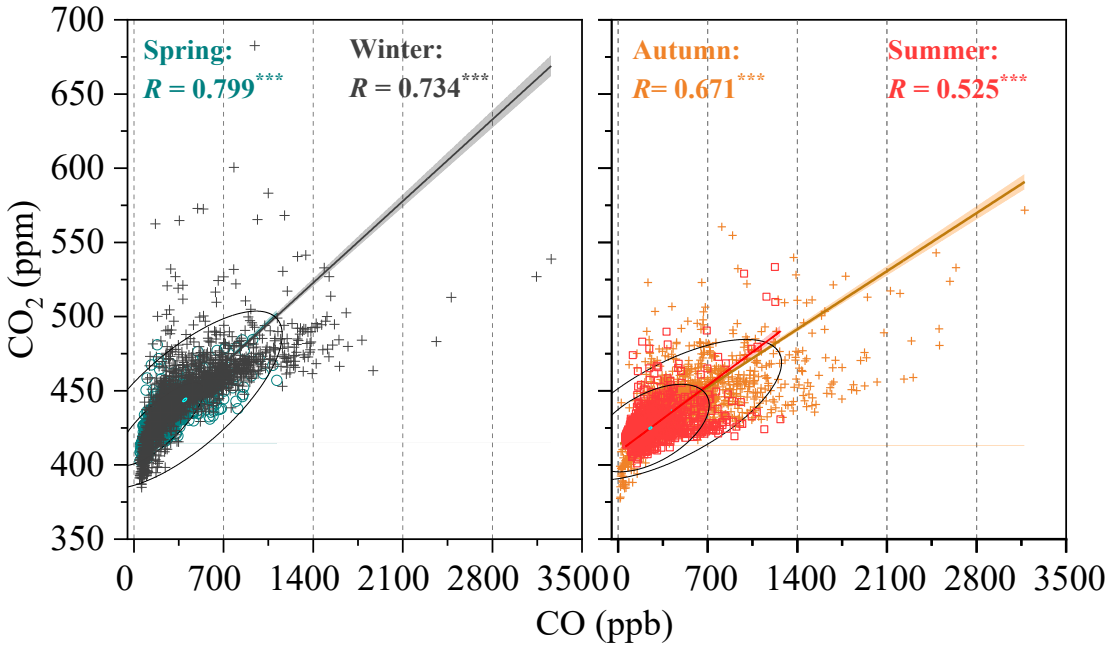

Figure S12: Correlations of concurrent CO_2 and CO measurements of different seasons at SHT site.

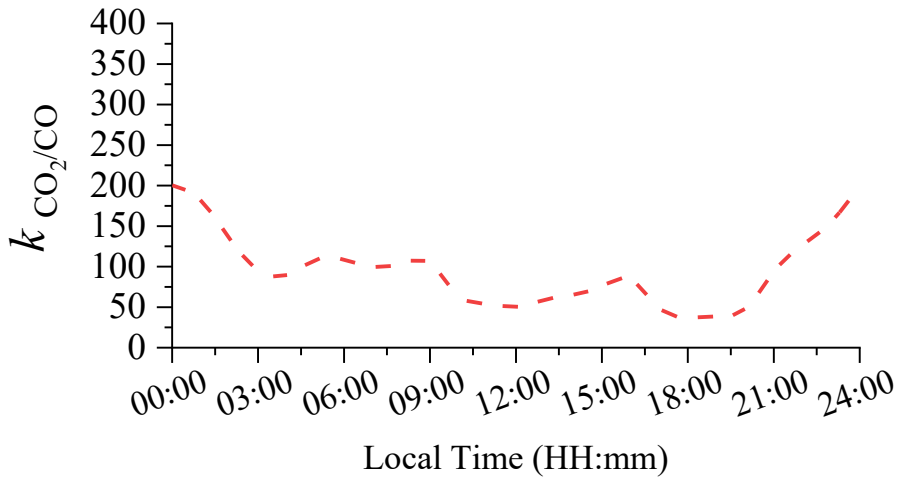

Figure S13: Time-dependent $k_{CO_2/CO}$ as a function of local time in summer for the SHT site.

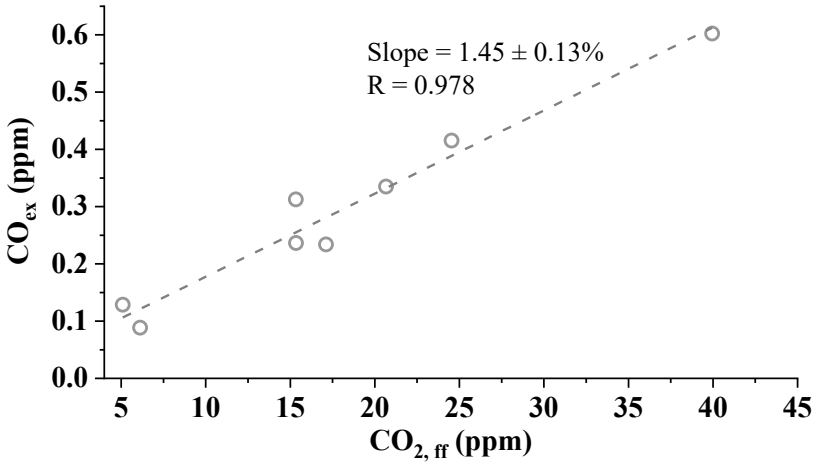

Figure S14: Correlations between the mole fractions of excess CO (CO_{ex}) and fossil fuels-derived CO_2 ($CO_{2, ff}$) at the site of Hengxiwu (HXW, 119.48°E, 30.60°N; 200 m a.s.l.) in the Yangtze River Delta (YRD) region. The CO_{ex} was estimated relative to the background station WLG, representative of the Northern Hemisphere mid-latitude interior. The $CO_{2, ff}$ was quantified using the CO_2-$\Delta^{14}C$ method, according to Levin et al. (2003) and Vásquez et al. (2022).

References

Chen, Y., Lu, Y., Qi, B., Ma, Q., Zang, K., Lin, Y., Liu, S., Pan, F., Li, S., Guo, P., Chen, L., Lan, W., and Fang, S.: Atmospheric CO_2 in the megacity Hangzhou, China: Urban-suburban differences, sources and impact factors, Sci. Total Environ., 926, https://doi.org/10.1016/j.scitotenv.2024.171635, 2024.

Levin, I., Kromer, B., Schmidt, M., and Sartorius, H.: A novel approach for independent budgeting of fossil fuel CO_2 over Europe by $^{14}CO_2$ observations, Geophys. Res. Lett., 30, https://doi.org/10.1029/2003GL018477, 2003.

Park, C., Jeong, S., Shin, Y.-s., Cha, Y.-s., and Lee, H.-c.: Reduction in urban atmospheric CO_2 enhancement in Seoul, South Korea, resulting from social distancing policies during the COVID-19 pandemic, Atmos. Pollut. Res., 12, 101176, https://doi.org/10.1016/j.apr.2021.101176, 2021.

Vásquez, M., Lara, W., Valle, J. I. D., and Sierra, C.: Reconstructing past fossil-fuel CO_2 concentrations using tree rings and radiocarbon in the urban area of Medellín, Colombia, Environ. Res. Lett., 17, 055008, https://doi.org/10.1088/1748-9326/ac63d4, 2022.

Ye, J., Zhang, Y., Yao, W., Liu, H., Lei, S., Zhang, Y., Zhang, J., Li, S., Lv, S., Wu, L., Tang, X., Sun, Y., Xin, J., Li, J., Wang, Z., Liu, L., Su, H., and Pan, X.: Significant shift of footprint patterns and pollutant source contributions: insights from observations at Shanghuang observatory, East China, Environ. Res. Lett., 19, https://doi.org/10.1088/1748-9326/ad8369, 2024.

Zhao, Z., He, Q., Lu, Z., Zhao, Q., and Wang, J.: Analysis of atmospheric CO_2 and CO at Akedala atmospheric background observation station, a regional station in Northwestern China, Int. J. Environ. Res. Public Health, 19, https://doi.org/10.3390/ijerph19116948, 2022.